JACS
JOURNAL OF THE AMERICAN CHEMICAL SOCIETY

ARTICLE

pubs.acs.org/JACS

The Atomic Structural Dynamics of γ-Al_2O_3 Supported Ir−Pt Nanocluster Catalysts Prepared from a Bimetallic Molecular Precursor: A Study Using Aberration-Corrected Electron Microscopy and X-ray Absorption Spectroscopy

Matthew W. Small,[†] Sergio I. Sanchez,[†] Laurent D. Menard,[‡] Joo H. Kang,[†,§] Anatoly I. Frenkel,[*,⊥] and Ralph G. Nuzzo[*,†]

[†]School of Chemical Sciences and the F. Seitz Materials Research Laboratory, University of Illinois, Urbana, Illinois 61801, United States

[‡]Department of Chemistry, University of North Carolina, Chapel Hill, North Carolina 27599, United States

[§]The Dow Chemical Company, Midland, Michigan 48667, United States

[⊥]Physics Department, Yeshiva University, New York, New York 10016, United States

Supporting Information

ABSTRACT: This study describes a prototypical, bimetallic heterogeneous catalyst: compositionally well-defined Ir−Pt nanoclusters with sizes in the range of 1−2 nm supported on γ-Al_2O_3. Deposition of the molecular bimetallic cluster $[Ir_3Pt_3(\mu\text{-}CO)_3(CO)_3(\eta\text{-}C_5Me_5)_3]$ on γ-Al_2O_3, and its subsequent reduction with hydrogen, provides highly dispersed supported bimetallic Ir−Pt nanoparticles. Using spherical aberration-corrected scanning transmission electron microscopy (C_s-STEM) and theoretical modeling of synchrotron-based X-ray absorption spectroscopy (XAS) measurements, our studies provide unambiguous structural assignments for this model catalytic system. The atomic resolution C_s-STEM images reveal strong and specific lattice-directed strains in the clusters that follow local bonding configurations of the γ-Al_2O_3 support. Combined nanobeam diffraction (NBD) and high-resolution transmission electron microscopy (HRTEM) data suggest the polycrystalline γ-Al_2O_3 support material predominantly exposes (001) and (011) surface planes (ones commensurate with the zone axis orientations frequently exhibited by the bimetallic clusters). The data reveal that the supported bimetallic clusters exhibit complex patterns of structural dynamics, ones evidencing perturbations of an underlying oblate/hemispherical cuboctahedral cluster−core geometry with cores that are enriched in Ir (a result consistent with models based on surface energetics, which favor an ambient cluster termination by Pt) due to the dynamical responses of the M−M bonding to the specifics of the adsorbate and metal−support interactions. Taken together, the data demonstrate that strong temperature-dependent charge-transfer effects occur that are likely mediated variably by the cluster−support, cluster−adsorbate, and intermetallic bonding interactions.

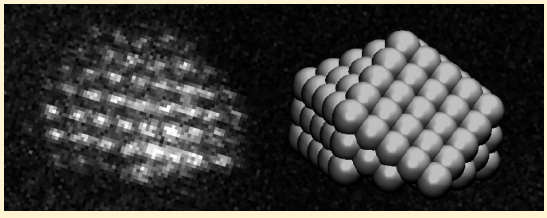

INTRODUCTION

In recent years, the characterization of nanoscale catalysts in basic energy-related research, especially as it regards their structural dynamics under operating conditions, has proven to be a frontier challenge.[1−4] Significant research efforts have established important, but incomplete, guidance as to the nature of atomistically rationalized structure-rate relationships for several important classes of heterogeneously catalyzed reactions.[3,5,6] These findings in some regards follow those developed in the more extensive literature on catalysis carried out on single-crystal surfaces.[3,7,8] It has been shown, for example, that the nature of an exposed crystal facet (i.e., (111), (011), etc.) on a nanoparticle can bias the chemistry that occurs at the surface and give rise to varying products.[9−11] The oxidation of styrene by Ag nanoparticles, as a specific example, proceeds on the (001) facets at a rate that is significantly higher than that seen on the (011) or (111) facets.[11] This notable example illustrates the larger requirement of understanding a nanoparticle's atomic scale features that might in turn serve to rationalize aspects of its catalytic properties.

In most important commercial processes, the catalytic materials present in supported form can be chemically quite complex—multimetallic compositions, complex structural and chemical promoters, alloying components, and multifunctional supports being some examples.[3,6,12−15] The modification of supported metallic heterogeneous catalysts with secondary metals is especially important as it provides a common strategy for improving catalytic activity, selectivity, and stability.[15−23] The performance improvements obtained over supported monometallic catalysts have been attributed variously to such features as the alteration of

Received: November 8, 2010
Published: February 22, 2011

the particle's structural and electronic properties that occurs upon alloying with a second metal.[22,24,25] Though catalytic applications of such materials has garnered considerable attention in research,[5,16−21,23,26−34] much of our mechanistic understanding of enhanced performance remains qualitative at best.

A variety of techniques have been used to characterize supported nanoparticle catalysts of this type.[35,36] Electron microscopy, when used in conjunction with energy dispersive X-ray spectroscopy (EDX), is particularly useful and provides means through which to establish such attributes as catalyst particle size, dispersion, and elemental composition.[35,36] Electron diffraction has been intensively exploited to assess the nature of the crystalline habits that are present in nanostructures, doing so with facility in systems with metal clusters as small as 2−3 nm.[37,38] More recently however, C_s-STEM has offered stunning results in the characterization of nanocrystal morphologies— measurements providing the most explicit depictions of the atomic structural attributes of heterogeneous catalytic materials.[39−41] As we and others have shown[1,42,43] the latter data are complimented by characterizations developed using XAS, which provides quantitative information about electronic structure and the local atomic bonding environments surrounding specific elements in a cluster, as well as a more qualitative description of its geometry.[44−46] Measurements of the X-ray absorption near edge structure (XANES) and extended X-ray absorption fine structure (EXAFS) regions of these spectra, more explicitly reveal the nature of specific oxidation states, coordination environments, bond distances, and structural coherency that are present in an ensemble of catalytic clusters.[44−46] The literature now richly demonstrates the synergies that develop when direct structural probes, such as electron microscopy, are used in tandem with such spectroscopic capabilities.[2,16,47−49] The present report extends this synergistic coupling to a detailed investigation of the structural dynamics evidenced in an exemplary heterogeneous catalytic system, Ir−Pt bimetallic nanoclusters supported on γ-Al_2O_3.

In an earlier report, we described the synthesis and atomic level structural characterization of polymer-stabilized Pt and Pd nanoparticles, including clusters with alloy and core/shell motifs, using C_s-STEM and theoretical simulations.[40] In that work it was determined that monometallic nanoparticles of Pt and Pd adopt diverging 3-D crystalline morphologies at the smallest size regime studied (∼1−3 nm). The significance of that work is that it demonstrated the exceptional capacities for structural characterization afforded by quantitative analytical electron microscopy measurements made at atomic resolution. For the materials considered in that study, *Z*-contrast microscopy provides a means for imaging, counting, and speciating atoms in a nanocluster with single-atom precision. Crystal truncations, defects, shape anisotropies, facet systems, and atomic segregation in the binary phases are among the different classes of information that measurements of this type can provide. These materials, systems of interest for electrocatalysis[17,18,26], have several advantages that favor C_s-STEM studies, not the least of which are the significant *Z*-contrasts afforded by binary Pt−Pd cluster compositions and their distinction from the relatively low-*Z* scattering background provided by the thin stabilizing polymer layers. In this respect, these compositionally, and morphologically, well-defined (essentially homogeneous) cluster catalysts provide a number of important contrasts to the more complex heterogeneous catalysts studied here. Most notable of these complexities are the absence of a *Z*-contrast between the Ir and Pt constituents as well as the more significant backgrounds contributed by the alumina support.

Here we examine the atomic and electronic structures of a supported bimetallic catalyst that closely models systems broadly used in hydrocarbon reforming processes: Ir−Pt particles supported on γ-Al_2O_3.[20,32] The incorporation of Ir into Pt/γ-Al_2O_3 petroleum refining catalysts has been shown to enhance the stability of the catalyst. In part, this is a result of the hydrogenolytic activity of Ir, which lowers the rate of coke deposition on the Pt metal catalysts.[24,32,50] It has also been suggested that specific support interactions can lead to improvements in catalyst regeneration.[6] In general terms, the diverse form of the impacts that have been found in systems like this are ones that are difficult to explain through a mere additive combination of each metal's attributes. The collaborative interplay of geometric and electronic effects must arise as a consequence of specific forms of atomic bonding.[40,51] Their effects, in turn, would be further impacted by the interactions of the metal cluster surfaces with both adsorbates and the support.[42,52,53] In almost every respect, the atomic-level bonding important in these contexts remains poorly understood.

To aid the characterization efforts of this work we adopted a synthetic approach to the Ir−Pt system that yields supported binary clusters—one based on the use of molecular precursors to prepare Ir−Pt heterogeneous catalysts with narrow size and compositional distributions.[54,55] Herein we describe the preparation of compositionally controlled Ir−Pt nanoparticles supported on γ-Al_2O_3 using the molecular precursor $[Ir_3Pt_3(\mu\text{-}CO)_3(CO)_3(\eta\text{-}C_5Me_5)_3]$.[56] The C_s-STEM micrographs made of the resultant nanoparticles show that these clusters are dispersed evenly over the support surface even at total metal weight loadings as high as 10% and that the individual particles retain the 1:1 Ir to Pt stoichiometry of the precursor. We find that the supported particles exhibit complex, environmentally responsive structural dynamics. Collectively, the data suggest that the clusters adopt quasi-phase-segregated core−shell structures that are further impacted by non-bulk-like, environmentally sensitive atomic relaxations. The broader structural features evidenced in Ir−Pt/γ-Al_2O_3, and atomic strains embedded within them, are also found to strongly track specific atomic level structural features of the support, as deduced from quantitative analyses of the C_s-STEM data.

EXPERIMENTAL METHODS

Ir−Pt/γ-Al_2O_3 Nanoparticle Preparation. The molecular cluster $[Ir_3Pt_3(\mu\text{-}CO)_3(CO)_3(\eta\text{-}C_5Me_5)_3]$ was synthesized in a manner previously described in literature.[57] The precursor cluster has a very strong affinity for the γ-Al_2O_3 support and rapidly adsorbs from a toluene solution. In order to achieve a more controlled deposition for a sample with a total metal loading of 10% by weight, the precursor was deposited by four successive treatments from dilute cluster solutions. To a stirred suspension of 500 mg of γ-Al_2O_3 (220 m^2/g, Alfa-Aesar) in 10 mL of toluene was added 21.5 mg of the Ir_3Pt_3 cluster compound (FW = 1735.65 g/mol) dissolved in 30 mL of toluene. After the mixture had been stirred for 3 h, the cluster had qualitatively adsorbed onto the support. The colorless supernatant was decanted, and a fresh solution (21.5 mg cluster in 30 mL toluene) was added to the γ-Al_2O_3, and the same procedure followed. Two additional treatments (20 mg cluster in 30 mL toluene) required stirring times of 14 and 20 h, respectively, to achieve the same level of deposition. The supported clusters were collected on a medium glass frit, washed with 30 mL of toluene, and dried under vacuum. The sample was heated under a reducing atmosphere in an in situ XAS sample cell in order to generate the supported Ir−Pt nanoparticles (see details below).

X-ray Absorption Spectroscopy Experimental Technique. Argonne National Laboratory's beamline 33-BM at the Advanced

Photon Source was used for acquisition of all XAS data. A pellet of the 10 wt % Ir−Pt/γ-Al_2O_3 sample was pressed at 4 tons and then mounted in an in situ EXAFS cell. Spectra were collected in transmission mode at the Ir L_3 edge (11215 eV) from 200 eV below the edge to 310 eV above the edge and at the Pt L_3 edge (11564 eV) from 200 eV below the edge to 1200 eV above the edge. The 310 and 1200 eV values for the Ir L_3 and Pt L_3 spectra were determined by the onset of the Pt L_3 and Ir L_2 absorption edges, respectively. Despite the presence of the Pt L_3 edge in the Ir L_3 EXAFS region most of the Ir EXAFS data was recovered by deconvoluting it from the Pt L_3 edge EXAFS as described in ref 57. The same procedure was used to separate Pt L_3 edge EXAFS from the total signal that contains also Ir L_3 edge EXAFS. A three-ion chamber setup was used in which the sample was mounted between ion chambers measuring either the incident beam intensity (I_0) or the transmitted beam intensity (I_t). The appropriate experimental standard (7 μm thick Pt foil or a pressed pellet of Ir black diluted with C black) was mounted between I_t and a reference ion chamber (I_r). This three ion chamber configuration allows for the simultaneous acquisition of the standard spectra and absolute energy alignment of the sample spectra. Gaseous mixtures used for the detection chambers were: 100% N_2 (I_0); 60% Ar, 40% N_2 (I_t); and 100% Ar (I_{ref}). The desired energy range was selected using a Si(111) double-crystal monochromator and focused using Pd-coated mirrors to reject higher harmonics. The storage ring was operated at 7 GeV with a constant ring current of 101.1 ± 0.4 mA (operated in top-up mode). Our final beam size was 1 mm × 8 mm.

The sample cell was purged with H_2 (4%, balance He), and the temperature was raised to 673 K. Subsequent reduction of the precursor cluster was monitored by measuring the Pt L_3 absorption edge and noting the decrease in the white line intensity to a steady-state. After reduction was complete, the temperature was lowered to 573 K, and full EXAFS scans over the energy regions noted above were made at both the Ir L_3 and Pt L_3 edges. The temperature was then lowered, and measurements at both edges were taken at 423, 293, and 215 K. Once this series of measurements under a H_2 atmosphere was completed, the sample was heated to 673 K, and the feed gas was switched to ultrahigh purity He. Desorption of the hydrogen was monitored by measurement of the Pt L_3 edge. Once the white line no longer exhibited perturbations in intensity, the temperature was decreased to 573 K, and measurements of the Pt and Ir edges were taken. Spectra were also collected at both edges for temperatures of 423, 293, and 215 K. Three spectra were measured at each edge for a given temperature/atmosphere combination for signal averaging purposes as well as to ensure that no structural changes were occurring during the measurements.

XAS Data Analysis. For this work, the interface programs Athena and Artemis,[58] which implement the FEFF6 and IFEFFIT codes,[59,60] were used to analyze the XAS data. The EXAFS oscillations, $\chi(k)$, were obtained from the absorption edge profiles using the background removal method AUTOBK.[61] In the present work, analysis of the EXAFS data is limited to first nearest neighbor (1NN) scattering paths since they are well-isolated from longer scattering paths in the Fourier transforms of the function $\chi(k)$. To separately analyze the local environments of Pt and Ir in the nanoparticle, we had to address the issue of the overlapping Ir L_3 and Pt L_3 edges to make full use of the information contained within the data. Our analysis consists of simultaneously fitting both the Ir L_3 and Pt L_3 oscillations while taking into account three spectral contributions: (1) the Ir EXAFS in the Ir L_3 edge, (2) the Pt EXAFS in the Pt L_3 edge, and (3) the Ir EXAFS in the Pt L_3 edge. Because (1) and (3) result from the same Ir coordination environment, they are strictly correlated. In this work, we performed simultaneous data analysis of the Pt and Ir edges using a new method recently developed by our group[57] to extract the data from the overlapping contributions of the absorption edges. The end result of this analysis is that the Ir EXAFS is analyzed over the full acquisition range except for a small gap of ~1.5 $Å^{-1}$ centered on the Pt L_3 edge, where the steep rise in the absorption obscures the EXAFS details. The passive electron reduction factors were determined from Pt foil and diluted Ir black standards. A total of 10 variables were used in the two-edge fit, a value that was well below the 22 relevant, independent data points.

For all of the analyses described in this article, the theoretical photoelectron paths used were calculated by FEFF6 for Pt−Pt and Ir−Ir 1NN scattering in the bulk fcc structures. Since it was not possible to discern between the 1NN Pt and Ir scattering centers using EXAFS (their scattering amplitudes and phase shifts are very similar), we obtained the effective Pt−M and Ir−M (where M = Pt or Ir) structural information: coordination numbers, bond lengths, and their disorder parameters. The coordination numbers were determined to be temperature-independent, within their uncertainties (Supporting Information (SI) Figure 1), thereby indicating that no large structural changes were occurring over the course of the experiments. As a result, it was possible to further refine the fitting analysis by fitting different data sets concurrently, over multiple measurement temperatures and constraining the temperature-independent variables (coordination number (N) and shift in edge energy (ΔE_0)) while varying the temperature-dependent variables (bond distance (R), mean squared bond length disorder, also known as the EXAFS Debye−Waller factor (σ^2) and the third cumulant ($\sigma^{(3)}$)).[2] Interested readers will find complete R-space 1NN fits of the data for both Ir and Pt bulk standards as well as the clusters under H_2 and He at all temperatures; and calculated EXAFS values in the Supporting Information (SI Figures 2−4 and SI Tables 1−2).

Scanning Transmission Electron Microscopy. Samples for scanning transmission electron microscopy (STEM) were prepared by depositing supported nanoparticle samples on a holey carbon film supported on a Mo grid (SPI Supplies). No solvent was used, so as to minimize contamination, and a Mo grid was employed because its EDX spectrum is featureless near the Ir and Pt L_α lines used in the quantitative elemental analysis. Low magnification imaging, HRTEM, NBD, and EDX spectroscopy were performed on a JEOL model 2010F electron microscope equipped with an Oxford INCA 30 mm^2 ATW detector for EDX spectroscopy. The instrument was operated at 200 keV with an electron probe beam focused to 0.5 nm for EDX analysis. In order to acquire EDX spectra from individual particles, sweeping of the probe beam was stopped while it was incident on a particle. Slight adjustments of the sample position were necessary to counteract drift during the several minutes required to acquire spectra with a satisfactory signal-to-noise ratio. To prevent signal contributions from neighboring particles, only well-isolated particles were selected for EDX analysis. Atomic resolution images were taken in STEM mode using a JEOL model 2200FS electron microscope capable of sub-ångstrom resolution[62] operated at 200 keV. All micrographs were analyzed using DigitalMicrograph (Gatan Inc.) software.

Although radiation damage and elemental restructuring may occur due to irradiation by the electron beam, the particles and support in the acquisition area appeared unchanged after acquisition of a micrograph. Although it is possible that repartitioning of the elements may occur within individual clusters under the 200 keV electron beam, as we explain below, Ir and Pt atoms are indistinguishable from one another due to the support-originated background.

Atom Counting. Quantification of the number of atoms contained within a cluster was carried out by calculating averaged single-atom scattering intensities for free atoms observed on the γ-Al_2O_3 support and measuring their background-corrected intensity contribution against the total intensity of an individual cluster (also background corrected). A similar protocol was implemented in a previous work.[40]

RESULTS

STEM images show that controlled reduction of the precursor cluster, $[Ir_3Pt_3(\mu\text{-}CO)_3(CO)_3(\eta\text{-}C_5Me_5)_3]$, affords Ir−Pt nanoparticles that are well dispersed on the γ-Al_2O_3 support (Figure 1, SI Figure 5) with an average diameter of 1.7 ± 0.5 nm (Figure 1b)

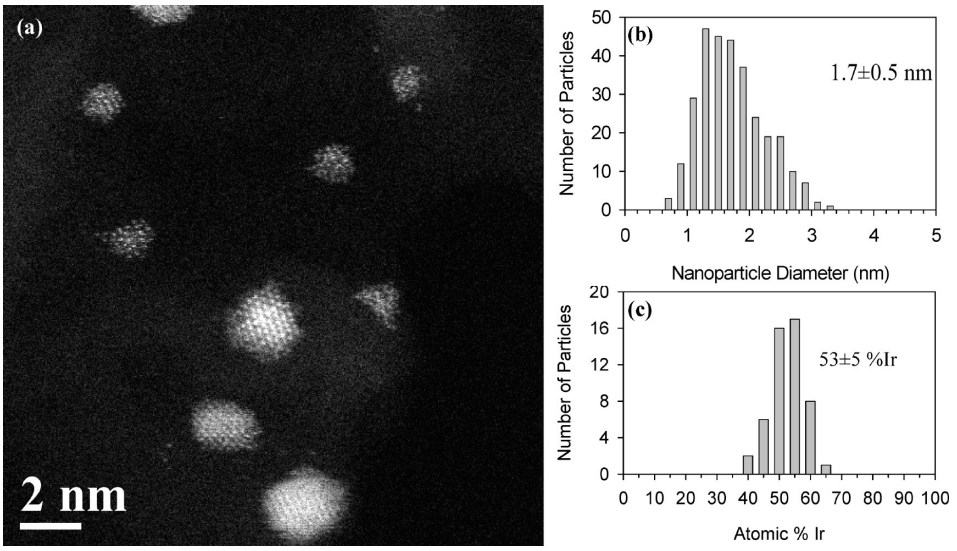

Figure 1. (a) Representative C_s-STEM image of 10 wt % Ir−Pt/γ-Al_2O_3 at 1 M × magnification. (b) Size distribution histogram of nanoparticle diameters obtained from analysis of individual particles in the microscopy images (300 particles analyzed). (c) Compositional distribution histogram of the elemental constituents of 50 individual nanoparticles as obtained using EDX.

and free of larger agglomerates. Inspection of Figure 1a shows that some particles exhibit crystalline features while others of similar size assume more disordered habits. Examination of multiple images shows that some atomic defects, in the form of a relatively sparse population of supported single atoms, are also present. This latter population is also represented in Figure 1a. The most important point of note here is that the mass fraction of these metal species is exceptionally small relative to the mass fraction of metal atoms present in the clusters. They are, therefore, expected to negligibly contribute to the XAS data, since it represents an average over all habits weighted by their mass fraction.

The presence of single, supported metal atoms allows a more precise, quantitative analysis of a typical cluster's morphology to be made. Here it is assumed that: (1) the background intensities of the region containing the cluster and free atoms are approximately equal; and (2) the elemental ratio of the single atoms used to find an average scattering value is equal to the elemental ratio within the cluster. The results of EDX measurements support the latter assumption, where an examination of the composition of 50 individual nanoparticles (average size of 1.9 ± 0.4 nm, Figure 1c) found that the clusters contained an average of 53 ± 5% Ir. This value lies within the limits of uncertainty of the 50% Ir value anticipated on the basis of the cluster precursor's stoichiometry and showed no compositional size dependence. On the basis of this finding we can conclude that individual, free atoms are equally likely to be either Ir or Pt. By calculating a background corrected scattering of individual atoms and clusters, atom quantification[40] was performed (Figure 2a) for 33 individual supported Ir−Pt nanoclusters. The visible trend indicates that the clusters likely adopt a hemispherical cuboctahedral habit. This is a structural assignment that is fully supported by the representative micrograph given in Figure 2b, which displays several individual particles oriented orthogonal to the optic axis, such that a cross-sectional vantage of the particle−support interface can be observed. Several nanoparticles displaying the inferred hemispherical geometries are clearly evidenced (here circled to highlight the prevalence of this structural form).

The C_s-STEM image presented in Figure 2b suggests several features of interest that relate to the nature of specific support interactions that might in fact drive correlated patterns of strain/structural relaxations in the supported clusters. These effects appear to be related to specific truncations of the polycrystalline γ-Al_2O_3 lattice, the surfaces on which nucleation and growth of the Ir−Pt metallic clusters proceeds. We found many regions of highly regular corrugations of the background intensity that had spacings well matched to specific *d*-spacings of the γ-Al_2O_3 bulk lattice. Due to the comparatively low *Z* nature of the support atoms (Z_{Al} = 13 and Z_O = 8), it is likely that any support ordering evidenced in the micrographs must correlate with highly aligned atomic columns in order to yield a cumulative intensity that is significant enough to discriminate and then usefully compare to the intensity modula seen due to the ordering of atoms present in the Ir−Pt nanoparticles. We have taken from the larger data set several examples that better emphasize specific periodic structures of the γ-Al_2O_3 support and the atomic arrangements of clusters bound on/near them. These data are given in Figure 3a and b, where an intensity profile of the boxed region has been inset into each micrograph to better illustrate the structural corrugations of the support that are present within the image field. Parts c and d of Figure 3 show atomistic models of the γ-Al_2O_3 oriented along the [001] zone axis (i.e., perpendicular to the e-beam). The arrows indicate the direction of the electron beam (i.e., the direction from which the micrograph would have been acquired) while the dashed lines show the atoms giving rise to the corrugations observed in the C_s-STEM images.

Fourier transforms were used to calculate the real space distance between the corrugation planes. Analysis yielded an interplanar spacing of 2.7 ± 0.1 Å for Figure 3c and 1.97 ± 0.02 Å for Figure 3d. These values compare very favorably with the *d*-spacings expected for (022) and (004) in γ-Al_2O_3 crystals (2.797 and 1.978 Å, respectively).[63] Observation of these planes is not surprising, as the (011) and (001) surfaces were previously identified as those most frequently exposed on the surface of γ-Al_2O_3.[43,64] While this allows us to identify the type of planes present, the relatively weak scattering of the support does not allow for facet or zone axis identification of the γ-Al_2O_3 with respect to the electron beam.

Although the C_s-STEM-based micrographs provide some structural information, they are limited by the sub-ångstrom

dx.doi.org/10.1021/ja110033g |*J. Am. Chem. Soc.* 2011, 133, 3582–3591

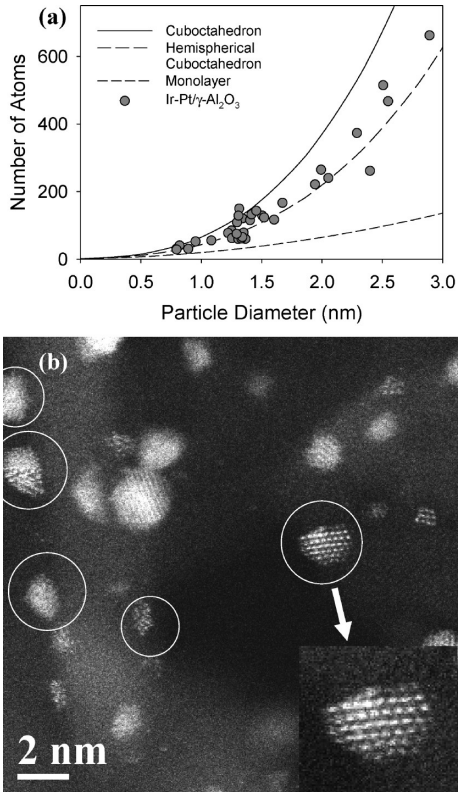

Figure 2. (a) Plot showing the number of atoms contained in a cluster as a function of the diameter. Lines represent ideal, fcc structures with a diameter taken as the average of the short and long axes (i.e., vertex-to-vertex and face center-to-face center). The circles represent data obtained by measuring individual particles. Total atom count estimates for these particles were obtained by measuring background-corrected, single-atom scattering intensities and extrapolating to the background-corrected cluster intensity. (b) C_s-STEM image showing multiple particles (circled for clarity) that appear to present a hemispherical cuboctahedral structure. The inset in the lower right-hand corner shows a magnified view of one of these clusters.

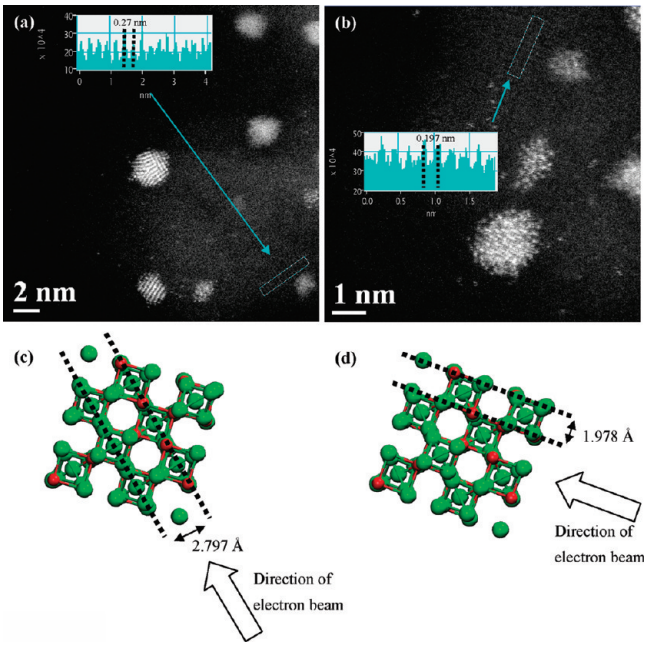

Figure 3. C_s-STEM images showing Ir−Pt clusters supported on sections of γ-Al_2O_3, displaying discernible lattice structures. The light blue, boxed regions represent where real intensity scans were conducted. These inset scans more clearly show the periodic scattering intensity originating from the underlying support. The planar spacings are 2.7 Å for image (a) and 1.97 Å for image (b). These values compare favorably with the values of 2.797 Å and 1.978 Å expected for the (022) and (004) *d*-spacings of γ-Al_2O_3, respectively. (c) and (d) are crystal models oriented along the [100] zone axis (i.e., perpendicular to the electron beam) depicting how the structure of a γ-Al_2O_3 crystal could give rise to corrugated intensities in (a) and (b), respectively. The direction of the electron beam is represented by arrows, and the dotted line indicates a plane of collimated atoms that would lead to the observed intensity increases. Al atoms are shown in green, while O atoms are depicted in red.

probe's depth of field. In contrast, HRTEM utilizes phase contrast to simultaneously image large areas of the sample. Captured HRTEM images (e.g., SI Figure 6) reveal that multiple domains of the γ-Al_2O_3 are present. To better characterize the nature of the polycrystalline γ-Al_2O_3 support, we took NBD measurements on random areas of the sample to identify the predominant zone axes of the support. It should be noted that the sizes of the areas where diffraction patterns were collected were ~20 nm^2, well surpassing the dimensions of an average 1.7 nm diameter Ir−Pt particle. This rules out the possibility of a single particle dominating the acquired diffraction pattern in a crystalline support-containing region. The majority of the NBD data collected for the support evidenced multiple crystallographic orientations and thus could not be indexed uniquely. There were occasions, however, when one orientation dominated and allowed a specific zone axis to be assigned (e.g., SI Figure 7). Within these diffraction patterns, orientations of [002], [022], and [004] were exhibited with corresponding *d*-spacings of 3.95, 2.80, and 1.97 Å; values also observed frequently in crystalline Ir−Pt clusters (e.g., Figure 3a and b).

Figures 4a and b display the XANES data collected for the Ir L_3 and Pt L_3 absorption edges, respectively, measured at a series of temperatures. These measurements were carried out first in an atmosphere of a 4% molar mixture of H_2 (balance in He) and, subsequently, in ultrahigh purity He. These data show that a red shift in the edge energy occurs with increasing temperature − one that is more pronounced for the Pt than the Ir atoms in the clusters. To better represent and quantify the effects of the surrounding gases, the ΔE_o from the XANES spectra was plotted for the Ir-edge (Figure 4c) and the Pt-edge (Figure 4d) where the data at 573 K under He at each respective edge was taken as the reference value. It can be seen that the Pt-edge position is the one more strongly perturbed by exposure to H_2 with a displacement ranging between +0.22 eV and +0.47 eV. Conversely, the Ir displacement under 4% H_2 attains a maximum offset of only +0.15 eV from the data collected under He.

Figure 5 shows the temperature-dependence of σ^2 plotted with respect to bulk standards for both the Ir- (Figure 5a) and Pt-edges (Figure 5b). Regression lines are plotted through the data points and extrapolated down to 0 K to qualitatively illustrate trends for the σ^2 values. The latter provide a qualitative means of assessing the disorder exhibited by each metal relative to the bulk standard. A clear similarity of the sample's temperature-dependent evolution of σ^2 to the Ir standard (and its dissimilarity to the Pt standard) suggests unique vibrational constraints are present in the heterometallic clusters, ones we will discuss the significance of below.

Lastly, the temperature-dependent 1NN bond length measurements of the Ir−Pt/γ-Al_2O_3 system along with those of the

dx.doi.org/10.1021/ja110033g |*J. Am. Chem. Soc.* 2011, 133, 3582–3591

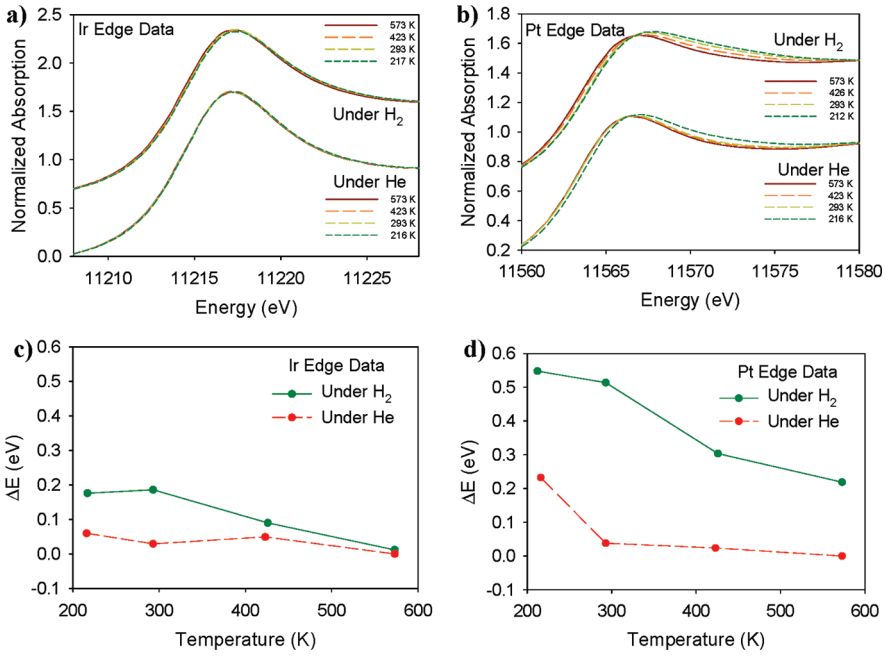

Figure 4. XANES data of the (a) Ir L_3 and (b) Pt L_3 absorption edges measured at a series of temperatures under He and 4% H_2 atmospheres. (c) and (d) show the shifts in the L_3 absorption edge energy (at a normalized intensity of 0.5) for Ir and Pt, respectively, relative to their edge energies under He at 573 K.

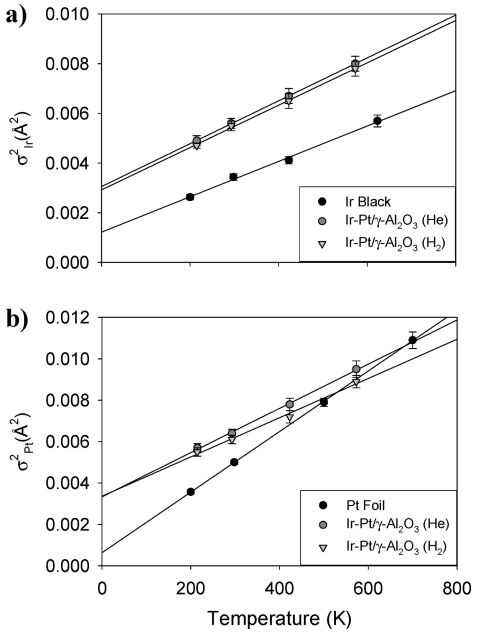

Figure 5. Mean square relative displacement of the 1NN distances found for the Ir−Pt/γ-Al_2O_3 as a function of temperature and surrounding gas determined for (a) Ir absorbers and compared to an Ir black standard and for (b) Pt absorbers and compared to a Pt foil standard.

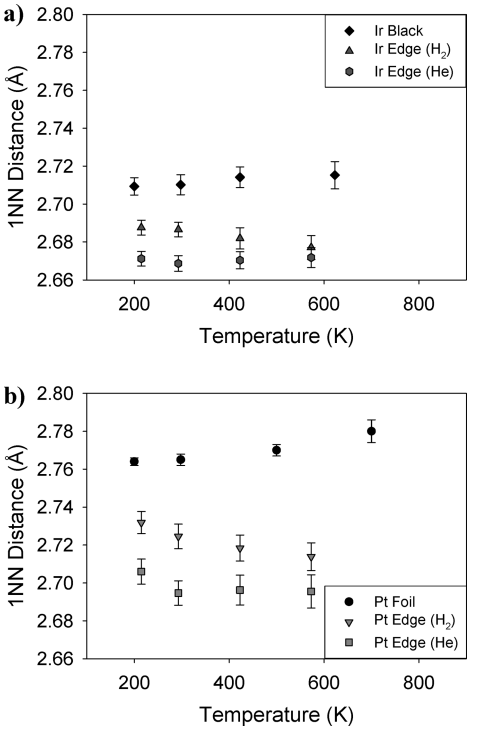

Figure 6. Temperature dependence of the 1NN interatomic bond distances for (a) Ir and (b) Pt atoms in Ir−Pt/γ-Al_2O_3 under H_2 and He compared to their respective standards.

corresponding thin, bulk standards are shown in Figure 6 (SI Tables 1 and 2). EXAFS fitting analyses of the Ir- and Pt-edge data at room temperature indicates that switching the sample's environment from H_2 to He results in a 1.07% contraction (relaxation) of the Pt−M 1NN distances. In comparison, the Ir 1NN distances show a contraction of only 0.64%. The varied (adsorbate-mediated) lifting of these contractions, as occurs upon exposure to H_2, is also visible in the data presented in Figure 6. This effect has been observed previously in studies of supported Pt clusters and ascribed to electron donation from hydrogen adsorbates.[65−67] We also make note of the temperature-mediated

dx.doi.org/10.1021/ja110033g |*J. Am. Chem. Soc.* 2011, 133, 3582–3591

changes in R_{Ir} and R_{Pt}. It is obvious that the Pt and Ir bulk standards both experience conventional thermal expansion, whereas the Ir−M and Pt−M 1NN bond lengths contract upon heating, a phenomenon that also has been previously observed for Pt/γ-Al_2O_3.[42,65] This striking mesoscopic behavior is one with origins related to specific (and competing) influences of both metal−adsorbate and metal−support bonding interactions, factors that are discussed more fully below.

■ DISCUSSION

Several lines of argument drawn from the data strongly suggest that the motif of a typical Ir−Pt cluster on γ-Al_2O_3 is one defined by an oblate/hemispherical shape. Most directly, the representative images in Figure 2 show several examples of clusters oriented to provide a profile view. These clearly reveal examples of clusters with hemispherical/oblate shapes, within which atomic order is also evidenced. On a broader and more qualitative inspection of the data given in Figures 2 and 3, it is also evident that other forms of oblate cluster shapes are present within the ensemble. Taken together, the data demonstrate a significant interaction with the support must be present, one sufficient to elicit nonspherical cluster shapes as well as drive/or inhibit specific forms of atomic ordering.

Perhaps the most striking feature of the data shown in Figure 3 is evidence of clusters with atomic orderings that seem to mirror orientations of the support. This is most evident in the micrograph shown in Figure 3b wherein the intensity modula seen in the inset (corresponding to (004), 1.97 Å, *d*-spacings) correlate very strongly with the atomic structure exhibited by the Ir−Pt cluster (displaying a [001] zone axis). Depending on the specifics of the surface termination, growth habits of this nature will involve periodic interactions of the cluster atoms with Al (or O) atoms on the γ-Al_2O_3 surface. Kwak, et al.[43] have provided evidence supporting the idea that the particle−support interface involves a topology wherein cluster atoms bond to only one type of support atom through their demonstration that Pt is anchored at pentacoordinate Al sites in Pt/γ-Al_2O_3. Such models do not fully address the role that surface defects (especially oxygen atom vacancies) might play within this bonding. It should be noted that if heteroepitaxial growth does indeed occur for the Ir−Pt nanoparticles on this orientation of the γ-Al_2O_3 support, there will be a ∼5% lattice mismatch for its interaction with a (001) facet plane of the cluster.

We propose that an important bonding mode of the Ir−Pt clusters on γ-Al_2O_3 is one that is heteroepitaxial in nature for the predominant facet planes (i.e., (001) and (011)) as judged by the frequencies with which these zone axes were observed for both the clusters and the support. An explicit example of this specific bonding habit is clearly demonstrated in Figure 3b, which shows an example where both the support and cluster are oriented along the same zone axis. We must caution, though, that the observation of such orientations of particles lying directly above these specific support corrugations does not definitively prove that the interfacial facet of the alumina and the particle are the same (the observation of a given *d*-spacing only establishes that the direction of observation is perpendicular to that *d*-spacing). As noted above, a heteroepitaxial bonding arrangement at the (001) facet of γ-Al_2O_3 would need to accommodate ≤5% mismatch between the support and fcc metal lattice constants. For clusters with an interaction occurring on a (011) facet (SI Figure 8) similar lattice strains would also be present. In the case of the specific orientation shown in Figure 3b, the interatomic distances between the terminal O atoms on the γ-Al_2O_3 compare favorably with the atomic spacing of the (001) plane of an Ir−Pt cluster. As noted above, however, O-vacancies are expected to represent a significant number of surface defects which, in turn, would lead to heterogeneity in both the bonding environments and energetics for the metal−support interactions. The literature and our past theoretical studies indicate that strong anchoring of the clusters may occur at these vacancy sites.[68] Clusters bound at O-vacancy sites would likely experience more interfacial strain than their heteroepitaxial counterparts. For small clusters, increasing levels of strain typically lead to decreased crystallinity in a manner similar to the introduction of twin boundaries.[38,69]

In an earlier report on structural habits adopted in Pt/Pd binary clusters we used atom counting techniques to deduce an average cluster morphology.[40] In that case, it was possible to make specific assignments as to the speciation of atoms within the clusters due to the significant *Z* contrasts these elements provide. Though C_s-STEM has proven to be a powerful technique for the elemental analysis for these latter systems, the similar scattering power of Ir and Pt (Z_{Ir} = 77 and Z_{Pt} = 78) (even without the presence of the interfering background of a support) obviates a C_s-STEM analysis of this system on the basis of contrast variations.[70] However, by adopting a similar average scattering intensity for the Ir and Pt atoms and (assuming a weak variation of the average background-scattering interactions around the clusters) using the proximal single atom defects to calibrate the detector response,[70] it is possible to predict and quantify a functional form for the size scaling of different cluster structural forms.[40] The quantitative atom-counting analysis, in this case, best supports a structure resembling an ideal oblate structure, more specifically that of an oblate/hemispherical cuboctahedron (Figure 2a).

Although this conclusion agrees with inferences developed from a visual inspection of the micrographs and the generally accepted morphology of supported clusters,[2] we have further substantiated these assignments through the use of XAS. In this case, analytical fitting of the EXAFS data (SI Tables 1 and 2) provides average Ir and Pt 1NN coordination numbers, with values for the 1.7 nm average diameter clusters examined here of 9.4 ± 0.2 and 6.8 ± 0.3, respectively. Several striking features are evident in these results. First, the fact that the coordination numbers of the Ir and Pt atoms are not equal, given that they reside in a sample characterized by a narrow size distribution and a 1:1 elemental composition, explicitly demonstrates atomic, intracluster segregation occurring in these clusters. We return to this point below. We start first, however, with a morphological interpretation of this data following the procedures developed in earlier works[2,54,55] and more recently reviewed by Frenkel.[71]

For a cluster containing two atom types with mole fractions x_A and x_B (for elements A and B, respectively), the average metal−metal coordination number is simply related to the partial coordination numbers (*n*) of A-M and B-M such that:

$$n_M = x_A n_{AM} + x_B n_{BM} \quad (1)$$

Because the nanoparticles have a 1:1 composition (x_A = x_B = 0.5), it follows that n_M (the average, noncompositionally dependent first shell coordination number) is simply the average of 9.4 and 6.8 (i.e., n_M = 8.1). This average value provides a parameter to evaluate various models of the particle shape. For a model hemispherical cuboctahedron [assuming a (011) basal plane][72]

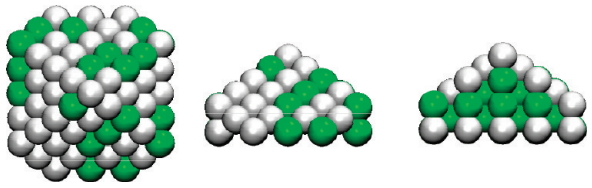

Figure 7. Schematic representation of a 110 atom, 1.7 nm Ir−Pt nanoparticle truncated by a (011) plane and possessing a hemispherical cuboctahedron morphology. From left to right, the images present views of the supported cluster viewed: perpendicular to the support, parallel to the support, and a cross section (to show the interior) of the cluster viewed parallel to the support. Pt atoms are depicted in white, and Ir atoms are shown in green.

an average coordination number for a 1.7 nm diameter cluster is $N = 7.9$, a value that is exceptionally close (and within the experimental uncertainty) to that determined by EXAFS (8.1 ± 0.3) and reaffirms the proposed structure.

An explicit model for a 1.7 nm cluster containing a 1:1 composition of each atom type, a 110-atom hemispherical cuboctahedral cluster whose average coordination number ($n_M \approx 7.9$) closely matches that found experimentally for the Ir−Pt nanoparticles, was modeled (Figure 7). As noted above, the compositionally dependent coordination numbers for Ir−M and Pt−M are different from this (9.4 and 6.8, respectively). This requires that, on average, the Pt atoms in an Ir−Pt (1:1) cluster must be allocated to lower coordination sites than are the Ir atoms. For a metal particle of this size, this requires a significant partitioning of the Ir to the cluster's core, as is schematically depicted in Figure 7. Here the Pt atoms shroud the Ir core from the ambient/nonsupport environment. This model yields a cluster core consisting of 30 atoms covered by an outer shell of 80 atoms (including the 31-atom (011) basal plane). If a 1:1 composition is to be maintained for this structural model, it is clear that some Ir atoms must be placed on the surface.

The XAS data also provides evidence that the phase-segregated structure of the Ir−Pt clusters is accompanied by discernible dynamical impacts on their electronic structure. Most notably, Figure 4b shows that a marked red shift in the absorption edge energy occurs for the Pt-edge with increasing temperature independent of the ambient conditions. These trends are also seen for the Ir data as well, albeit significantly smaller in their magnitudes. A quantitative interpretation of the broader trends (e.g., red shift) evidenced in the XANES data requires deconvolution of the various competing factors involved, namely those due to adsorbate and cluster−support interactions, the varied influences of temperature on bonding as well as the influences due to the presence of an alloying metal. It must be noted that the constant displacement of the Pt edge data under 4% H_2 as compared to He (Figure 4d) reveals information about the elemental apportionment of Pt in the supported clusters. Over the temperature range investigated, we estimate the hydrogen coverage will range between ~13% at 573 K to 100% at 212 K for 4% H_2 (SI Calculation 1). The marked change in the Pt XANES data when any level of adsorbate is present indicates Pt atoms experience direct-contact interactions with adsorbate atoms. The fact that the adsorbate effect on Ir-edge data is much weaker than on Pt data is consistent with a greater tendency for Pt to segregate to the surface of the particle and agrees with the conclusions reached on the basis of the EXAFS results.

For the specific case of the Ir−Pt bimetallic nanoparticles, the Pt atoms are expected to populate the surface of the clusters on the basis of the differences in surface energy ($\gamma_{Pt} = 2.489$ J/m^2 and $\gamma_{Ir} = 3.048$ J/m^2).[73] The literature, which reveals other instances where surface energetics have been shown to play a pivotal role in elemental segregation, supports this inference. In one notable example, the deposition of Au on a single-crystal Ni surface was shown to result in the formation of Au−Ni alloys on top of the Ni surface, a process in which the specific atomic arrangements adopted are directed by the relative energetics of the Au and Ni near-surface bonding interactions.[74] Somorjai et al. have also shown that changes in surface energies caused by the presence of reactive species can lead to specific forms of elemental rearrangement within bimetallic nanoclusters.[75]

The XAS data provides further insights into the nature of the clusters' dynamics. For example, one notes that the temperature dependence of σ^2_{Ir} (Figure 5a) behaves similarly to its bulk analogue while the corresponding Pt-edge data deviates dramatically from its corresponding bulk standard (Figure 5b). Because the slope in a plot of σ^2 versus temperature over the range investigated has been shown (using an Einstein model[2,42]) to be inversely proportional to the force constant, a smaller slope can be interpreted as denoting a stiffer bonding environment. In this respect, the σ^2_{Ir} values follow a path more resembling that of the Ir black standard as might be expected from their predominant segregation to the particle core. Meanwhile the σ^2_{Pt} values indicate a bonding environment drastically different from fully coordinated Pt atoms present in the bulk state.

As previously noted, a quantitative evaluation of adsorbate coverage effects on the Ir−Pt/γ-Al_2O_3 clusters cannot easily be decoupled from effects rising from the support nor the alloying Ir. For example, there is a noticeable contrast seen in the behavior of each metal's white line intensity, with an increase occurring for Ir and a decrease occurring for Pt with increasing temperatures (Figures 4a,b). This is consistent with the occurrence of a temperature-dependent charge transfer from Ir to Pt in the nanoparticles. Similar temperature-dependent white line intensity trends have recently been observed, and similarly interpreted, for heterogeneous Au/Pt nanowires,[76] Au/Pt hybrid nanostructures,[77] and Au/Pt alloy nanoparticles.[78]

The 1NN bond lengths, as represented by the data presented in Figure 6, reveal an additional convolution of dynamical effects on structure. The bond-length contraction observed with increasing temperature has been seen in studies made on homometallic supported clusters (Pt).[42,65] This effect has its origins in the electronic interplay due to both the adsorbate bonding and the metal−support interactions. As illustrated in the data presented in Figure 6, the Pt−M and Ir−M bond distances both evidence mesoscopic temperature dependencies: relaxed bond lengths that contract as the temperature increases. One notes that the magnitude of the contraction is largest for the Pt−M bonding and further sensitive to the presence of H-atom adsorbates. The former, present at saturation, partially lifts the cluster's bond-length contraction and results in bond distances converging toward those found in bulk materials. At higher temperatures, where the H-coverage is lower, the Pt−M bond distances progressively contract. It is also interesting to note that the M−M′ bond lengths seen for both Ir and Pt in an inert atmosphere are always shorter than those found in the presence of H_2. In the present case, the thermally mediated influences due to the metal−support interactions are less pronounced than was seen in our studies of supported homometallic Pt clusters. We believe this likely reflects in part the predominant placement of the Pt atoms at the ambient cluster surfaces. While attractive

from a qualitative perspective, the data clearly demonstrate that the dynamical behaviors in the bimetallic system are intricate and subject to a more complex interplay of interactions. Even so, the major thermal influences on the M−M′ bond lengths seen in the H_2 atmosphere are likely ones attributable to the coverage dependence of H-atom adsorbates. The current data show the highly anisotropic nature of this effect, where the relaxation of surface atoms occurs toward the particle core with a magnitude that depends on the number of unsatisfied bonds each atom experiences.[38] The features of the bond-length contraction, and their sensitivity to adsorbates are likely common for many supported, high dispersion systems. We expect these dynamical features must also impact catalytic properties and elements of structure present under real operating conditions.

CONCLUSIONS

Advanced synthesis and characterization techniques have been combined to show that Ir−Pt nanoparticles supported on γ-Al_3O_3 containing a 1:1 ratio of Ir:Pt adopt segregated structures in which Ir occupies the core region and suggests a means by which to control the efficacy of catalyst synthesis. Observation of temperature- and adsorbate-dependent bond-length contractions, bond rigidity reflective of one element, and metal−metal charge transfer indicate that catalysts evolve dynamically through temperature- and adsorbate-mediated changes. Further comparison of model structures to the atomic structure of γ-Al_2O_3 showed that the corrugations in the intensity of the support matched well to spacings expected within the cluster and represent $\leq$5% strain if heteroepitaxial growth is occurring. We believe the methods of analysis used in the present work are more generally applicable to the investigation of supported materials and that the structural dynamics seen in the present model Ir−Pt system are ones likely to be found in other highly dispersed, supported metal systems. How these dynamics might come to influence elementary rate processes of catalytic reaction mechanisms remains an important and interesting challenge for future research.

ASSOCIATED CONTENT

Supporting Information. Additional microscopy images, XAS fits/results, models showing ideal facet structures/distances and how the hydrogen coverage change was estimated. This material is available free of charge via the Internet at http://pubs.acs.org.

AUTHOR INFORMATION

Corresponding Author
anatoly.frenkel@yu.edu; r-nuzzo@illinois.edu.

ACKNOWLEDGMENT

We thank A. J. Sealey and G. S. Girolami for synthesizing the organometallic, Ir−Pt precursor complex used in this work. This work was sponsored in part by a Grant from the U.S. Department of Energy (DE-FG02-03ER15476). Experiments were carried out in part at the Frederick Seitz Materials Research Laboratory Central Facilities, University of Illinois, which are partially supported by the U.S. Department of Energy under Grants DE-FG02-07ER46453 and DE-FG02-07ER46471. Research was also carried out at the Advanced Photon Source (APS) at Argonne National Laboratory. The use of the APS was supported by the U.S. Department of Energy, Office of Science, Office of Basic Energy Sciences (DE-AC02-06CH11357).

REFERENCES

(1) Billinge, S. J. L.; Levin, I. *Science* **2007**, *316*, 561.
(2) Frenkel, A. I.; Hills, C. W.; Nuzzo, R. G. *J. Phys. Chem. B* **2001**, *105*, 12689.
(3) Gates, B. C. *Catalytic Chemistry*; John Wiley & Sons, Inc.: New York, NY, 1992; p 458.
(4) Bukhtiyarov, V. I.; Slin'ko, M. G. *Russ. Chem. Rev.* **2001**, *70*, 147.
(5) Rase, H. F. *Handbook of Commercial Catalysts: Heterogeneous Catalysts*; CRC Press: Boca Raton, 2000.
(6) Satterfield, C. N. *Heterogeneous Catalysis in Industrial Practice*, 2nd ed.; McGraw-Hill, Inc.: New York, 1991.
(7) Rodriguez, J. A.; Goodman, D. W. *Surf. Sci. Rep.* **1991**, *14*, 1.
(8) Gates, B. C.; Knozinger, H. *Impact of Surface Science on Catalysis*; Academic Press: New York, NY, 2000; p 448.
(9) Chen, J.; Lim, B.; Lee, E.; Xia, Y. *Nano Today* **2009**, *4*, 81.
(10) Bratlie, K. M.; Lee, H.; Komvopoulos, K.; Yang, P.; Somorjai, G. A. *Nano Lett.* **2007**, *7*, 3097.
(11) Xu, R.; Wang, D.; Zhang, J.; Li, Y. *Chem. Asian J.* **2006**, *1*, 888.
(12) Sinfelt, J. H.; Via, G. H.; Lytle, F. W. *J. Chem. Phys.* **1982**, *76*, 2779.
(13) Koningsberger, D. C.; Oudenhuijzen, M. K.; Bitter, J. H.; Ramaker, D. E. *Top. Catal.* **2000**, *10*, 167.
(14) Koningsberger, D. C.; Oudenhuijzen, M. K.; de Graaf, J.; van Bokhoben, J. A.; Ramaker, D. E. *J. Catal.* **2003**, *216*, 178.
(15) Gjervan, T.; Prestvik, R.; Totdal, B.; Lyman, C. E.; Holmen, A. *Catal. Today* **2001**, *65*, 163.
(16) Christensen, S. T.; Feng, H.; Libera, J. L.; Guo, N.; Miller, J. T.; Stair, P. C.; Elam, J. W. *Nano Lett.* **2010**, *10*, 3047.
(17) Wang, J. X.; Inada, H.; Wu, L. J.; Zhu, Y.; Choi, Y.-M.; Liu, P.; Zhou, W.-P.; Adzic, R. R. *J. Am. Chem. Soc.* **2003**, *131*, 17298.
(18) Li, H.; Sun, G.; Li, N.; Sun, S.; Su, D.; Xin, Q. *J. Phys. Chem. C* **2007**, *111*, 5605.
(19) Hwang, B. J.; Kumar, S. M.; Chen, C.; Monalisa; Cheng, M.; Liu, D.; Lee, J. *J. Phys. Chem. C* **2007**, *111*, 15267.
(20) Sinfelt, J. H. *Bimetallic Catalysts: Discoveries, Concepts and Applications*; Wiley: New York, 1983.
(21) Ichikawa, M.; Rao, L.; Kimura, T.; Fukuoka, A. *J. Mol. Catal.* **1990**, *62*, 15.
(22) Guczi, L. *J. Mol. Catal.* **1984**, *25*, 13.
(23) Guczi, L. *Catal. Today* **2005**, *101*, 53.
(24) Anderson, J. A.; Garcia, M. F. *Supported Metals in Catalysis*; Imperial College Press: London, 2005.
(25) Gross, A. *Top. Catal.* **2006**, *37*, 29.
(26) Yang, J.; Lee, J. Y.; Zhang, Q.; Zhou, W.; Liu, Z. *J. Electrochem. Soc.* **2008**, *155*, B776.
(27) Aboul-Gheit, A. K.; Aboul-Fotouh, S. M.; Aboul-Gheit, N. A. K. *Appl. Catal., A* **2005**, *292*, 144.
(28) Chen, Y.; Yang, F.; Dai, Y.; Wang, W.; Chen, S. *J. Phys. Chem. C* **2008**, *112*, 1645.
(29) Michel, C. G.; Bambrick, W. E.; Ebel, R. H.; Larsen, G.; Haller, G. L. *J. Catal.* **1995**, *154*, 222.
(30) Miyake, T.; Asakawa, T. *Appl. Catal., A* **2005**, *280*, 47.
(31) Ortiz-Soto, L. B.; Alexeev, O.; Oleg, S.; Amiridis, M. D. *Langmuir* **2006**, *22*, 3112.
(32) Rasser, J. C.; Beindorff, W. H.; Scholten, J. J. F. *J. Catal.* **1979**, *59*, 211.
(33) Sarkany, A.; Zsoldos, Z.; Stefler, G.; Hightower, J. W.; Guczi, L. *J. Catal.* **1995**, *157*, 179.
(34) Yang, O. B.; Woo, S. I.; Kim, Y. G. *Appl. Catal., A* **1994**, *115*, 229.
(35) Goodhew, P.; Humphreys, J.; Beanland, R. *Electron Microscopy and Analysis*, 3rd ed.; Taylor & Francis: London, 2001; p 76.
(36) Williams, D. B.; Carter, B. C. *Transmission Electron Microscopy: Basics*; Springer Science+Business Media Inc.: New York, 1996.

(37) Zuo, J.; Gao, M.; Tao, J.; Li, B. Q.; Twesten, R.; Petrov, I. *Microsc. Res. Tech.* **2004**, *64*, 347.
(38) Huang, W. J.; Sun, R.; Tao, J.; Menard, L. D.; Nuzzo, R. G.; Zuo, J. M. *Nat. Mater.* **2008**, *7*, 308.
(39) Rosenthal, S.; McBride, J.; Pennycook, S.; Feldman, L. *Surf. Sci. Rep.* **2007**, *62*, 111.
(40) Sanchez, S. I.; Small, M. W.; Zuo, J.; Nuzzo, R. G. *J. Am. Chem. Soc.* **2009**, *131*, 8683.
(41) Ferrer, D.; Blom, D. A.; Allard, L. F.; Mejia, S.; Perez-Tijerina, E.; Jose-Yacaman, M. *J. Mater. Chem.* **2008**, *18*, 2442.
(42) Sanchez, S. I.; Menard, L. D.; Bram, A.; Kang, J. H.; Small, M.; Nuzzo, R. G.; Frenkel, A. I. *J. Am. Chem. Soc.* **2009**, *131*, 7040.
(43) Kwak, J. H.; Hu, J.; Mei, D.; Yi, C. W.; Kim, D. H.; Peden, C. H. F.; Allard, L. F.; Szanyi, J. *Science* **2009**, *325*, 1670.
(44) Teo, B. K. *EXAFS: Basic Principles and Data Analysis*; Springer-Verlag: Berlin, 1986.
(45) Koningsberger, D. C.; Mojet, B. L.; van Dorssena, G. E.; Ramaker, D. E. *Top. Catal.* **2000**, *10*, 143.
(46) Koningsberger, D. C.; Prins, R. *X-ray Absorption: Principles, Applications, Techniques of EXAFS, SEXAFS and XANES*; John Wiley & Sons: New York, 1988.
(47) Bayindir, Z.; Duchesne, P. N.; Cook, S. C.; MacDonald, M. A.; Zhang, P. *J. Chem. Phys.* **2009**, *131*, 244716.
(48) Rojas, T. C.; Sayagues, M. J.; Caballero, A.; Koltypin, Y.; Gedanken, A.; Ponsonnet, L.; Vacher, B.; Martin, J. M.; Fernandez, A. *J. Mater. Chem.* **2000**, *10*, 715.
(49) Cheng, G.; Carter, J. D.; Guo, T. *Chem. Phys. Lett.* **2004**, *400*, 122.
(50) Charron, A.; Kappenstein, C.; Guerin, M.; Paal, Z. *Phys. Chem. Chem. Phys.* **1999**, *1*, 3817.
(51) Rodriguez, J. A.; Goodman, D. W. *Science* **1992**, *257*, 897.
(52) Schneider, S.; Bazin, D.; Garin, F.; Maire, G.; Capelle, M.; Meunier, G.; Noirot, R. *Appl. Catal., A* **1999**, *189*, 139.
(53) Mojet, B. L.; Miller, J. T.; Ramaker, D. E.; Koningsberger, D. C. *J. Catal.* **1999**, *186*, 373.
(54) Nashner, M. S.; Frenkel, A. I.; Somerville, D. M.; Hills, C. W.; Shapley, J. R.; Nuzzo, R. G. *J. Am. Chem. Soc.* **1998**, *120*, 8093.
(55) Nashner, M. S.; Somerville, D. M.; Lane, P. D.; Adler, D. L.; Shapley, J. R.; Nuzzo, R. G. *J. Am. Chem. Soc.* **1996**, *118*, 12964.
(56) Feeman, M. J.; Miles, A. D.; Murray, M.; Orpen, A. G.; Stone, G. A. *Polyhedron* **1984**, *3*, 1093.
(57) Menard, L. D.; Wang, Q.; Kang, J. H.; Sealey, A. J.; Girolami, G. S.; Teng, X.; Frenkel, A. I.; Nuzzo, R. G. *Phys. Rev. B* **2009**, *80*, 064111.
(58) Ravel, B.; Newville, M. *J. Synchrotron Rad.* **2005**, *12*, 537.
(59) Rehr, J. J.; Zabinsky, S. I.; Albers, R. C. *Phys. Rev. Lett.* **1992**, *69*, 3397.
(60) Newville, M. *J. Synchrotron Rad.* **2001**, *8*, 322.
(61) Newville, M.; Livins, P.; Yacoby, Y.; Rehr, J. J.; Stern, E. A. *Phys. Rev. B* **1993**, *47*, 14126.
(62) Wen, J.; Mabon, J.; Lei, C.; Burdin, S.; Sammann, E.; Petrov, I.; Shah, A. B.; Chobattana, V.; Zhang, J.; Ran, K.; Zuo, J. M.; Mishina, S.; Aoki, T. *Microsc. Microanal.* **2010**, *16*, 183.
(63) Zhou, R.-S.; Snyder, R. L. *Acta Crystallogr., Sec. B* **1991**, *47*, 617.
(64) Xia, W. S.; Wan, H. L.; Chen, Y. *J. Mol. Catal. A: Chem.* **1999**, *138*, 185.
(65) Kang, J. H.; Menard, L. D.; Nuzzo, R. G.; Frenkel, A. I. *J. Am. Chem. Soc.* **2006**, *128*, 12068.
(66) Kampers, F. W.; Koningsberger, D. C. *Faraday Discuss. Chem. Soc.* **1990**, *89*, 137.
(67) Reifsnyder, S. N.; Otten, M. M.; Sayers, D. E.; Lamb, H. H. *J. Phys. Chem. B* **1997**, *101*, 4972.
(68) Vila, F.; Rehr, J. J.; Kas, J.; Nuzzo, R. G.; Frenkel, A. I. *Phys. Rev. B* **2008**, *78*, 121404/1.
(69) Gilbert, B.; Huang, F.; Zhang, H.; Waychunas, G. A.; Banfield, J. F. *Science* **2004**, *305*, 651.
(70) Iakoubovskii, K.; Mitsuishi, K. *J. Phys.: Condens. Matter* **2009**, *21*, 155402/1.
(71) Frenkel, A. I. *Z. Kristallogr.* **2007**, *222*, 605.
(72) Hardeveld, R.; Hartog, F. *Surf. Sci.* **1969**, *15*, 189.
(73) Vitos, L.; Ruban, A. V.; Skriver, H. L.; Kollar, J. *Surf. Sci.* **1998**, *411*, 186.
(74) Nielsen, L. P.; Besenbacher, F.; Stensgaard, I.; Laegsgaard, E.; Engdahl, C.; Stoltze, P.; Jacobsen, K. W.; Norskov, J. K. *Phys. Rev. Lett.* **1993**, *71*, 754.
(75) Tao, F.; Grass, M. E.; Zhang, Y.; Butcher, D. R.; Renzas, J. R.; Liu, Z.; Chung, J. Y.; Mun, B. S.; Salmeron, M.; Somorjai, G. A. *Science* **2008**, *322*, 932.
(76) Teng, X.; Feygenson, M.; Wang, Q.; He, J.; Du, W.; Frenkel, A. I.; Han, W.; Aronson, M. *Nano Lett.* **2009**, *9*, 3177.
(77) Teng, Z.; Han, W.; Wang, Q.; Li, L.; Frenkel, A. I.; Yang, J. C. *J. Phys. Chem. C* **2008**, *112*, 14696.
(78) Bus, E.; Van Bokhoben, J. A. *J. Phys. Chem. C* **2007**, *111*, 9761.